A&A 366, 106–120 (2001)
DOI: 10.1051/0004-6361:20000192

Astronomy & Astrophysics

Mid-infrared imaging and spectroscopy of the enigmatic cocoon stars in the Quintuplet Cluster⋆

A. Moneti[1], S. Stolovy[2], J. A. D. L. Blommaert[3], D. F. Figer[4], and F. Najarro[5]

[1] Institut d'Astrophysique, 98bis Blvd. Arago, 75014 Paris, France
e-mail: moneti@iap.fr
[2] CalTech, Astronomy Dept., 105-24, Pasadena, CA 91125, USA
e-mail: srs@astro.caltech.edu
[3] ISO Data Centre, PO Box 50727, 28080 Madrid, Spain
e-mail: Joris.Blommaert@esa.int
[4] Space Telescope Science Institute, 3700 San Martin Drive, Baltimore, MD 21218, USA
e-mail: figer@stsci.edu
[5] Instituto Estructura de la Materia, CSIC, Serrano 121, 29006 Madrid, Spain
e-mail: najarro@isis.iem.csic.es

Received 25 September 2000 / Accepted 26 October 2000

Abstract. In an attempt to determine the nature of the enigmatic cocoon stars in the Quintuplet Cluster, we have obtained mid-infrared imaging and spectrophotometry of the cluster, using the CAM and SWS instruments on ISO, using SpectroCam-10 on the Palomar 5 m telescope, and NICMOS on HST. The spectra show smooth continua with various dust and ice absorption features. These features are all consistent with an interstellar origin, and there is no clear evidence for any circumstellar contribution to these features. We find no spectral line or feature that could elucidate the nature of these sources. Detailed modeling of the silicate absorption features shows that they are best reproduced by the μ Cep profile, which is typical of the interstellar medium, with $\tau_{\rm sil} \simeq 2.9$. The high spatial resolution mid-IR images show that three of the five cocoon stars have spatially extended and asymmetric envelopes, with diameters of $\sim$20 000 AUs. A reddening law similar to that of Lutz (1999) but with silicate features based on the μ Cep profile and normalized to our value of $\tau_{\rm sil}$ is used to deredden the observed spectrophotometry. The dereddened energy distributions are characterised by temperatures of 750–925 K, somewhat cooler than determined from near IR data alone. Models of optically thin and geometrically thick dust shells, as used by Williams et al. (1987) for very dusty, late-type WC stars, reproduce the observed SEDs from 4 to 17 μm, and imply shell luminosities of $\log(L/L_\odot) \simeq 4.5$–4.9 for the brightest four components. An analysis of the various suggestions proposed to explain the nature of the cocoon stars reveals serious problems with all the hypotheses, and the nature of these sources remains an enigma.

Key words. galactic centre – quintuplet cluster – extinction – ISO

1. Introduction

The Quintuplet Cluster (AFGL 2004) is one of the three young clusters known in the vicinity of the Galactic Centre. It was first identified in the near infrared survey of Glass, Catchpole, & Whitelock (1987) as a bright source coincident with AFGL 2004, and found to be a bright IRAS source with a cool energy distribution (Glass 1988). It is located about 30 pc from the Centre in projection, and its cluster nature became apparent with the advent of IR cameras through the works of Glass et al. (1990, GMM90), Nagata et al. (1990), Okuda et al. (1990), Moneti et al. (1992), and Moneti et al. (1994 [MGM94]), who identified over a dozen stars in the cluster, including five with extraordinarily large luminosities ($\sim 10^5\ L_\odot$), cool (600–1200 K) energy distribution, and featureless K-band spectra. These characteristics led those authors to tentatively identify them as massive, dust-enshrouded young stars, henceforth *cocoon* stars. The possibility that they be OH/IR stars was discarded since (i) they have no CO bandhead at 2.3 and 4.6 μm, (ii) they show little or no variability (Glass et al. 1999 find peak-to-peak of $\sim 0.45 \pm 0.05$ mag and K for two of them, no

Send offprint requests to: A. Moneti

⋆ ISO is an ESA project with instruments funded by ESA Member States (especially the PI countries: France, Germany, The Netherlands and the UK) and with the participation of ISAS and NASA.

variability for the remainder), (iii) they lack OH maser emission, (iv) they are cooler and more luminous than typical OH/IR stars, and (v) they are much younger than OH/IR stars, assuming they are coeval with the cluster (≈4 Myr, Figer et al. 1999 [FMM99], Figer et al. 1999). More recently, FMM99 suggested that the cocoon stars might be extremely dusty, late-type WC stars (DWCL, Williams et al. 1987, WHT), even though they do not detect the expected emission features in the J-band. And finally, Glass et al. (1999) suggested they could be self-obscured, very massive O stars close to the ZAMS, which, according to Bernasconi & Maeder (1996), go through a prolonged accretion phase of 2–2.5 Myr, comparable to the age of the Quintuplet Cluster, before becoming visible.

In an attempt to elucidate the nature of the cocoon stars, we have obtained spectroscopy and spectrophotometry in the mid-IR, where these sources are brightest, in order to (i) search for spectral features intrinsic to the stars, (ii) obtain accurate measurements of their spectral energy distribution, (iii) to investigate their spatial extension, and (iv) to study the shape of the silicate feature in particular to determine whether it could be partly intrinsic to the sources.

2. Observations, calibration, and results

Two instruments onboard the Infrared Space Observatory (ISO, Kessler et al. 1996) were used: ISOCAM (Cesarsky et al. 1996) was used to obtain high spatial and low spectral resolution Circular Variable Filter (CVF) spectrophotometry of the Quintuplet Cluster from 2.5 to 17 μm, and SWS (de Graauw et al. 1996) was used to obtain two high resolution spectra at two positions in the cluster. Table 1 lists the ISO identification number (ION) of the datasets used. Of these, the last was proposed and planned by the authors, while the remainder were obtained by other investigators and taken from the archive. Some preliminary results based on the ION 09901781 dataset have already presented Nagata et al. (1996). Since that time, the calibrations have improved considerably and, in particular, the CVF spectral response function used here is based on stellar observations obtained in orbit, and differs considerably from the one used in Nagata et al. (1996), which was obtained on the ground prior to launch.

We also present high spatial resolution ground-based 8–14 μm spectroscopy and narrow-band imaging photometry of the cluster members, obtained with SpectroCam-10 on the Palomar 5 m telescope, and 1–2.5 μm photometry derived from HST/NICMOS images. These data are particularly useful to understand the limits of low spatial resolution ISO data.

2.1. SWS grating spectroscopy

The SWS spectra were obtained in the AOT1-speed 3 mode, which scans the grating continuously over its full range, and produces a number of spectral segments, corresponding to the various aperture/grating/detector

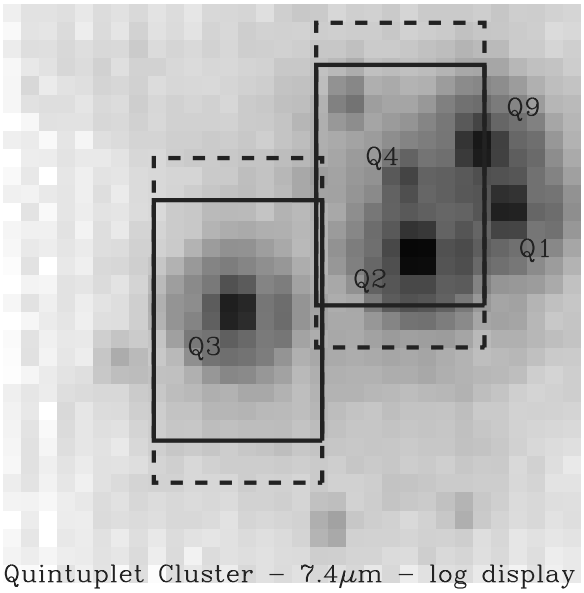

Fig. 1. Location of the SWS apertures on a 7.4 μm ISOCAM image of the Quintuplet Cluster. The intensity scale is logarithmic, north is up and east is to the left. The naming convention is that of GMM90. Solid line is aperture 1 ($14'' \times 20''$), and dashed lines is aperture 2 ($14'' \times 27''$). The source to the NE of Q4 was denoted Q5 in GMM90

Table 1. ISO datasets

ISO ION	Instr.	mode	date
09901781	CAM	C04 (CVF)	24-Feb.-96
28701246	SWS	S01-speed 3	29-Aug.-96
29702147	SWS	S01-speed 3	09-Sep.-96
84500303	CAM	C04 (CVF)	09-Mar.-98

combinations. These segments cover the full spectral range of 2.3–47 μm with a nominal resolving power ranging between 250 and 600. In this work we will be concerned primarily with data out to 28 μm, which were obtained with the two smallest apertures, which are nominally $14'' \times 20''$, $14'' \times 27''$, respectively, though in practice slightly larger [A. Salama, private communication]. The aperture changes at 12 μm. The location of the nominal apertures on a 7.4 μm images CVF image is shown in Fig. 1, where the cocoon stars are identified following the naming convention of Moneti et al. (1992). The SWS apertures were centered on Q4 and Q3 (respectively GCS 3-I and GCS 4 in Kobayashi et al. 1983).

Data processed with version 7.0.1 of the ISO Pipeline were further cleaned with ISAP[1] by removing data from noisy detectors, and, for each spectral segment, the data from the different detectors were normalized to the average of the complete set of data, effectively compensating

[1] The ISO Spectral Analysis Package (ISAP) is a joint development by the LWS and SWS Instrument Teams and Data Centers. Contributing institutes are CESR, IAS, IPAC, MPE, RAL and SRON.

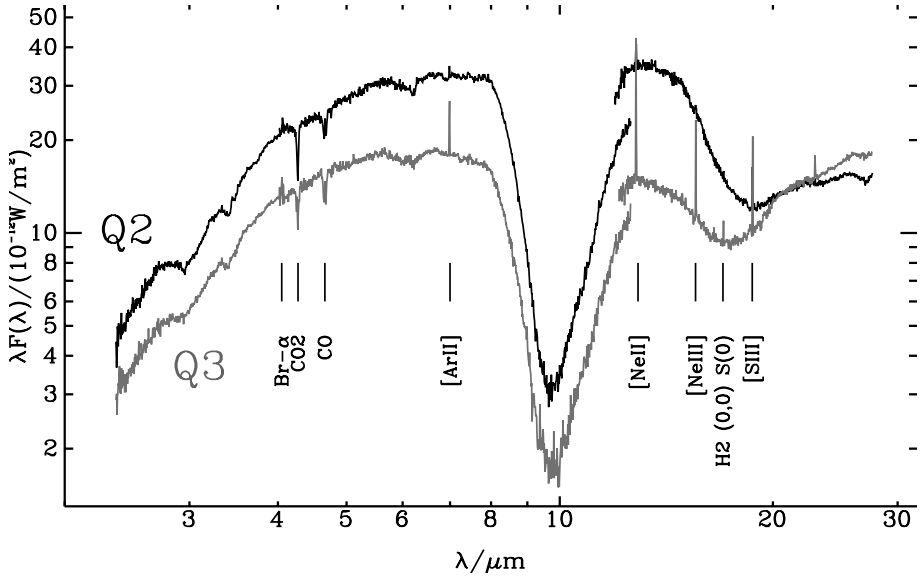

Fig. 2. SWS spectra of Q2 (primarily) and Q3. The jump at 12 μm corresponds to the aperture change; see text for details

for slight residuals in dark current (at low signals) or in detector responsivity (at high signals). Following these steps, the agreement between adjacent segments was quite good; the results are shown in Fig. 2. The jump at 12 μm is due to the change in effective aperture, and is expected when observing extended sources. At wavelengths beyond 28 μm the effective SWS apertures are even larger and they include a significant part of the Pistol H II region whose hot dust emission dominates the spectrum. These parts of the spectra will not be considered further.

The calibration used in the SWS Pipeline assumes that the target is point-like and in the center of the aperture. In that case, the nominal overall uncertainties would be ∼5% up to 4.1 μm, ∼10% for 4.1–27 μm, and ∼30% beyond 29 μm (see de Graauw et al. 1999 for details). This is essentially the case for Q3, which is sufficiently isolated from the other sources. In the case of the GCS-3 complex, which includes Q1, 2, 4, and 9, the aperture was centered on Q4, but the brightest source in the beam is Q2, located 6″ south of Q4, and significant light is scattered into the aperture from the other components, especially at long wavelengths, where the PSF is broadest.

2.2. CAM CVF imaging

The ISOCAM instrument, used to obtain CVF (Continuously Variable Filter) scans, contains two separate cameras that cover the regions shortward and longward of 5 μm (henceforth "SW" and "LW", respectively). Both cameras utilize 32×32 pixel arrays, an InSb array with CID readout for the SW channel and a Si:Ga array with a direct read-out for the LW channel. The spectral resolving power ranges from 45 to 100. For each CVF segment, a single scan was obtained with wavelength increasing with time, and each scan was preceded by a long (40–100) series of frames obtained at the first CVF position for detector stabilisation.

We present here 2.5–3.0 μm and 4–5 μm spectra from the ISO 09901781 dataset, and 5–17 μm spectra from the ISO 84500303 dataset. All these data were obtained with a pixel scale of 1.5″. The ISO 09901781 dataset also contains 5–17 μm data obtained with the 3 arcsec/pixel scale, but these data are, for the most part, heavily saturated, and are not discussed here. In both cases, the total integration time per spectral position was approximately 1 min.

For completeness we also examined the ISO 49400231 and the ISO 49400268 datasets, which contain 3×3 rasters of the cluster at two CVF positions and with two broad filters. The filter data suffer from significant saturation, and the CVF data are qualitatively of much lower quality than the complete CVF scans, probably as a results of transient effects during the raster scanning process.

The ISOCAM data were reduced and calibrated with the IDL-based CAM Interactive Analysis (CIA) package[2] following the standard steps of (i) dark subtraction, (ii) removal of cosmic ray events, (iii) correction of the behaviour of the detector in response to signal jumps (transient correction, LW only, using the "inversion" method), (iv) averaging all valid images obtained at a given CVF position, (v) flatfielding the results using library flats, and (vi) conversion the average signal to physical units using standard conversion factors, originally derived from several standard stars. Throughout the analysis, the dead column (#24) in the LW array was replaced by the average of the adjacent columns. No ghost image could be identified in the CVF data, nevertheless some light could be lost to low-level, diffuse ghost images. From a study of the background, sampled in the NE corner of the array, see Sect. 3.2, we find that the background level is 2% of

[2] CIA is a joint development by the ESA Astrophysics Division and the ISOCAM consortium, led by the ISOCAM PI, C. Cesarsky, Direction des Sciences de la Matière, C.E.A., France.

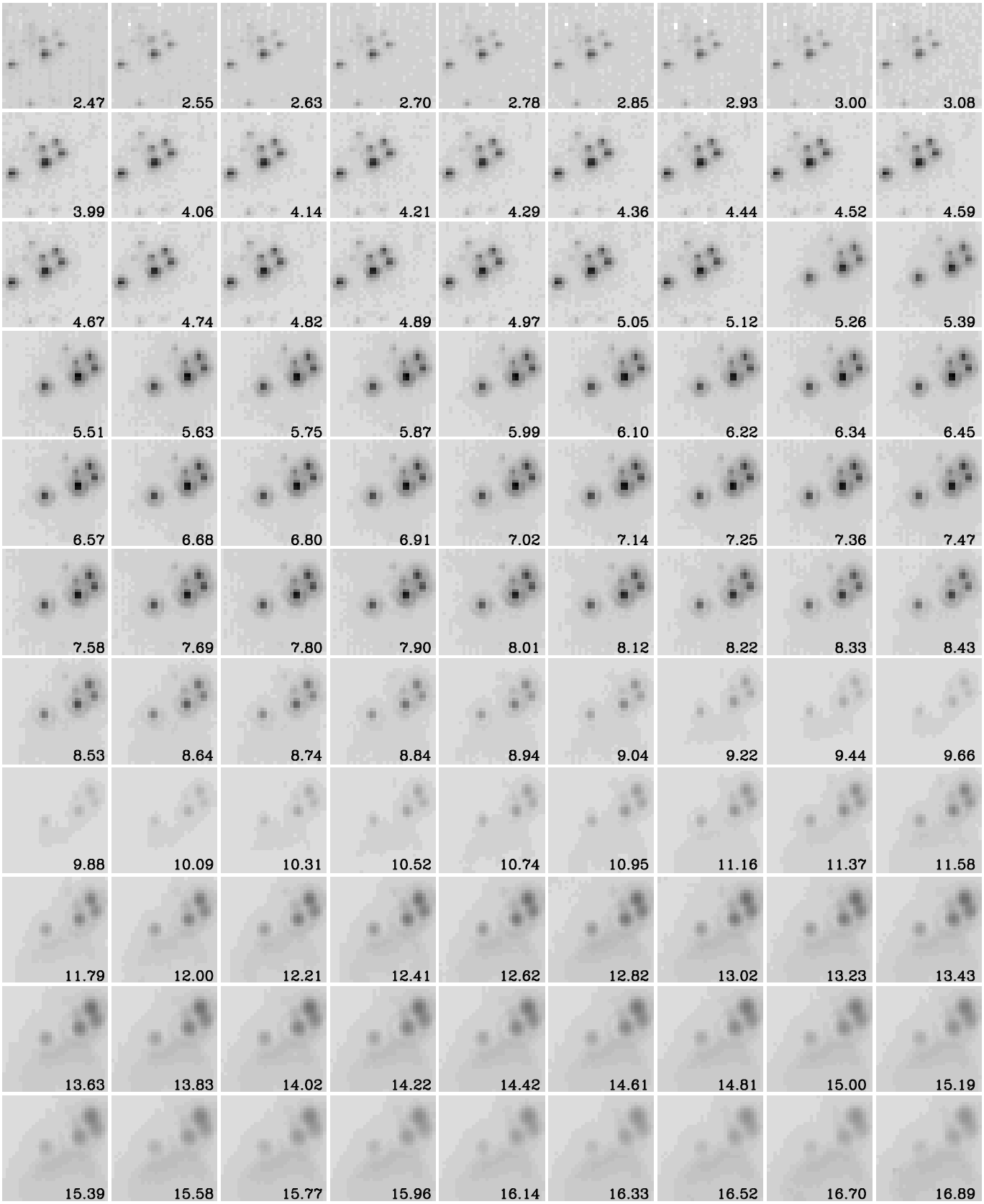

Fig. 3. Composite of most of the CVF images of the Quintuplet Cluster. Wavelengths in μm are labeled. Individual panels are normalized in $\lambda F(\lambda)$ units. North is up and east is to the left, and each panel is $48''$ on the side. The jump in image position between 5.12 and 5.26 μm is due to the switch from the SW to the LW section of ISOCAM

the total signal in the array at $\lambda < 6\,\mu$m, then rises quickly to 5% at $8\,\mu$m, and remains at that level thereafter.

A composite of the resulting data is shown in Fig. 3, where the individual panels are normalized in $\lambda F(\lambda)$ units. Note in particular (i) the nearly complete silicate absorption, (ii) that the brightest source at short wavelength, Q2, is no longer so at long wavelength, where Q9 becomes brightest, and (iii) the increase in PSF size with wavelength.

The nebula south of the cluster, which becomes prominent at $\lambda > 10\,\mu$m, is the Pistol nebula, and the Pistol star is prominent at the bottom of the frames at the short wavelengths. These are the subject of a separate paper (Moneti et al. 2000, in preparation).

The main difference between these results and those of Nagata et al. (1996) is that the spectral response function for the SW-CVF section ($\lambda < 4\,\mu$m) has changed considerably (Biviano et al. 1997), so that the new flux densities in the 2.5–3 μm range are now lower by almost a factor of 2, and the 3 μm ice feature is shallower than previously reported. As will be shown below, the new results are in better agreement with previously published results.

2.3. Palomar imaging and spectroscopy

High spatial resolution (1″) images and low-resolution ($R \sim 50$) spectra were obtained in the 8–13 μm atmospheric window with SpectroCam-10 (Hayward et al. 1993) on the Palomar 5 m Hale telescope. These observations were taken on July 10–12, 1993 (spectroscopy and 11.7 μm imaging) and June 14, 1995 (8.7 μm imaging). SpectroCam-10 uses a 128×128 Rockwell Si:As detector. Its camera mode has a fully illuminated field of view of ∼15″ diameter with 0.256″ pixels. All observations employed the standard mid-infrared techniques of chopping the secondary mirror (typically at 5–10 Hz) and nodding the telescope (typically 60″ E-W, every few minutes) in order to adequately subtract the thermal background. Images were obtained with two standard OCLI filters centered at 8.74 and 11.66 μm with half-power bandwidths of $\Delta\lambda = 0.78$ and 1.11 μm, respectively, and mosaics were constructed from these images. The flux calibrators were α Boo and α Her, and their fluxes were obtained from Hanner et al. (1984). An airmass correction was derived from observations of standard stars at different airmasses; the cocoon stars were observed at a typical airmass of 2.3.

Figure 4 represents a mosaic of 47 seeing-selected, flat-fielded 11.7 μm images, each with a total on-source integration time of 40 s. During the mosaic process the pixels were subsampled by factor of three in order to optimise image registration; after mosaicking, the images were rebinned back to the original pixel sizes, and the result was smoothed slightly with a Gaussian of $\sigma = 0.8$ pixel. A mask was used to omit pixels not fully illuminated. The image registration accuracy in the region containing the cocoon stars is estimated to be better than 0.3 pixles, or $\lesssim 0.1''$; in regions without bright stars, the telescope

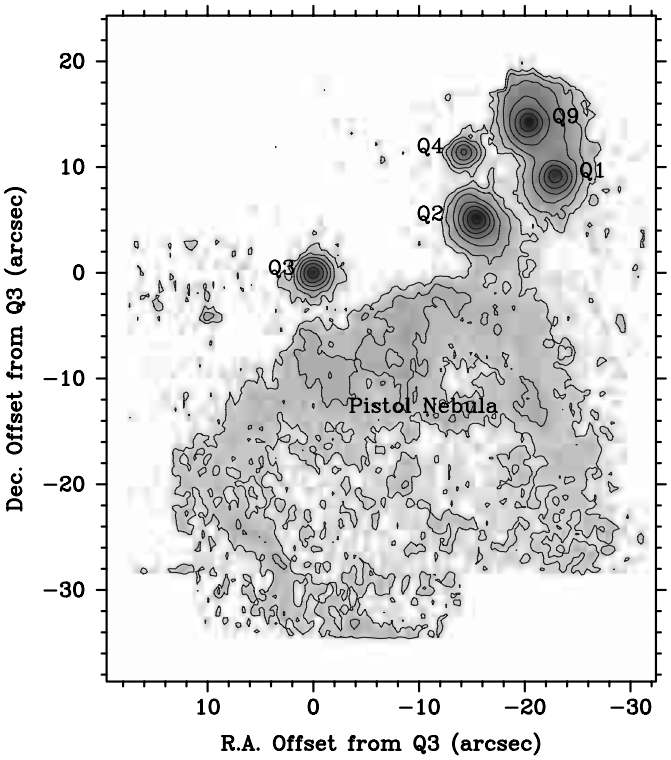

Fig. 4. Mosaic of the Quintuplet Cluster and the Pistol Nebula at 11.7 μm. Pixels are 0.256″ wide, the grey-scale is logarithmic to show the large dynamic range, and the contour levels are 1.3, 3.1, 8.0, 120 49, 123, and 311×10^{-14} W m^{-2} μm^{-1} arcsec^{-2} (0.05, 0.12, 0.31, 0.76, 1.9, 4.8, and 12.1 Jy arcsec^{-2})

offsets were used, and the registration accuracy is only ∼1″. The 8.7 μm image was constructed from 56 images with 5 seconds on-source integration time each.

The spectroscopy was obtained with a $2'' \times 15''$ slit to yield a resolution of $\lambda/\Delta\lambda \sim 50$. The slit was oriented N-S, the dispersion was 0.046 μm/pixel, and four pixels were combined for each resolution element. Four grating settings were used to cover to 8–13 μm range and each setting was exposed for a total integration time on-source of 20 seconds for each of the cocoon stars. Atmospheric lines were used for wavelength calibration and β Peg was observed for flux calibration and to correct for atmospheric lines.

2.4. HST/NICMOS imaging

The Quintuplet cluster was observed with NICMOS on HST in program 7364 in Sep. 1997 with Camera 2, giving a spatial resolution of 0.075″/pix. Three broadband filters were used: F110W, F160W, and F205W. Figer et al. (1999c) give details of the observations. The raw data were retrieved from the STScI archive and were re-reduced with an improved linearity correction algorithm using the "calnica" task in STSDAS. This had the effect of recovering photometric information for the central pixels of the Quintuplet stars, which were flagged as saturated in the pipeline data reduction. Mosaics were constructed

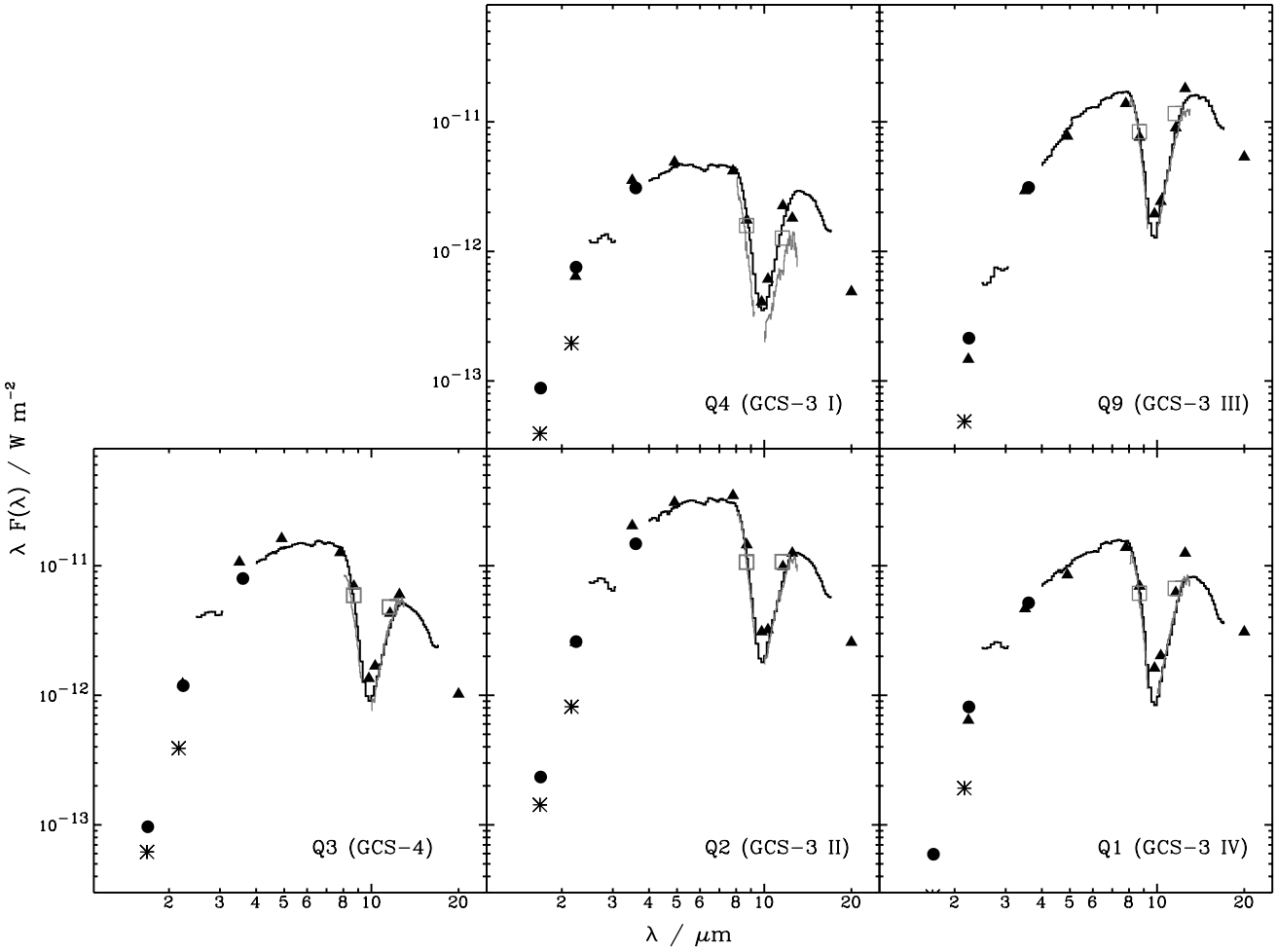

Fig. 5. Observed spectra and photometry of the cocoon stars. The J-band data and some H-band data were left off scale in order to avoid overly compressing the ordinate, which would make the spectral features too small to see (these data points are plotted in Fig. 11 below). The CVF spectra are the black histogram, Palomar spectra and photometry are grey histogram and squares, NICMOS photometry are asterisks. The circles are near-IR imaging photometry from FMM99, and triangles are mid-IR aperture photometry from Okuda et al. (1990). The panels show the sources roughly in their positions on the sky

by aligning 16 dithers in each filter to produce the final images. Residual dc levels were measured and subtracted from the images.

2.5. Photometric and spectrophotometric results

Photometry of the cocoon stars was extracted from each CVF image by integrating within a small aperture and multiplying the result by an aperture correction factor that was determined from CVF observations of the standard star δ Draconis. The sky background at each wavelength was determined from regions of the image free of stars, and the same sky level was used for all sources. Even with a small aperture the photometry of the faintest sources can suffer significant contamination from the wings of the brighter sources nearby. This effect is most serious at long wavelength where the PSF is largest. This problem is most acute for Q4, which is the weakest source and which is surrounded by three bright ones.

The SpectroCam-10 photometry was extracted with a 5–7″ (diameter) aperture, depending on the extendedness of the source. The NICMOS photometry was derived from the energy enclosed in a 3-pixel radius (0.45″ diameter) aperture, and then corrected to an infinite aperture using measured isolated stars to derive the aperture correction. These correction factors were 1.31, 1.50, and 1.71 for the F110W, F160W, and F205W filters, respectively. The results are listed in Table 2. We assign these values conservative uncertainties of 0.2 mag, which are due primarily to the photometric extraction method and to errors in the estimate of the residual dc levels. The actual uncertainty for the brighter sources is likely to be closer to 0.1 mag, especially at the longer wavelengths.

Conversion to flux densities are based on the system in which Vega (without its mid-IR excess) is assigned 0-mag in all bands (Cohen et al. 1992)[3] While conversion of

[3] The Vega model used for the absolute calibration can be found in `www.iso.vilspa.esa.es/users/expl_lib/ISO/wwwcal/isoprep/cohen/vega9605.dat`

Table 2. Photometry (in magnitudes) of the cocoon stars

Source	GCS	[F110W]	[F160W]	[F205W]	[8.7]	[11.7]
Q1	3-IV	16.63	11.48	8.37	1.14	0.13
Q2	3-II	14.46	9.71	6.80	0.54	−0.38
Q3	4	15.31	10.62	7.60	1.18	0.49
Q4	3-I	15.78	11.11	8.35	2.61	1.94
Q9	3-III	18.88	13.54	9.86	0.80	−0.46
$\lambda_{\rm iso}/\,\mu$m		1.14	1.63	2.10	8.69	11.55
A_λ/A_V		0.285	0.177	0.119	0.073	0.081
FZM$_\lambda$/Jy		1571	1075	695	50.4	28.9

magnitudes to flux densities is straightforward, the determination of the proper wavelength at which the flux density should be plotted is more complicated, since it depends on the shape of the (observed) energy distribution of the source. For this purpose, we have modeled the intrinsic shape of the 1–4 μm energy distributions as warm blackbodies, and reddened them with the reddening law discussed below to produce a model *observed* energy distribution. This was then used to compute the isophotal wavelength, $\lambda_{\rm iso}$, as defined by the relation

$$F(\lambda_{\rm iso}) \int T(\lambda){\rm d}\lambda = \int F(\lambda)T(\lambda){\rm d}\lambda,$$

where $F(\lambda)$ is the observed spectrum of the source, and $T(\lambda)$ is the transmission of the instrument (including filter, detector efficiency, optics, and possibly the earth's atmosphere). For $\lambda_{\rm iso}$ to be unique, $F(\lambda)$ must be a monotonic function of λ, which is indeed the case for our models. The isophotal wavelengths for the NICMOS and SpectroCam-10 filters are listed in Table 2 together with the values of reddening correction (A_λ/A_V) and the adopted flux density for a zero magnitude FZM$_\lambda$/Jy.

Figure 5 shows the observational results, which are compared with the ground-based photometry of FMM96 (filled circles) and of Okuda et al. (1990, filled triangles, see also corrections in Nagata et al. 1996). Approximate $\lambda_{\rm iso}$ values were computed for the FMM99 data using standard J, H, and K filter profiles, but not for the mid-IR data, which was obtained with narrow-band filters.

The agreement between the CVF and the Palomar spectra is excellent, as is the agreement between the CVF spectra and the ground-based photometry. The discrepancy between the CVF and the Palomar spectra of Q4 at $\lambda \gtrsim 10\,\mu$m is due to the contamination of the CVF spectrophotometry of Q4 by its bright neighbours (see above). We consider the CVF spectrum unreliable there, and will instead rely on the Palomar results.

At NIR wavelengths, the NICMOS fluxes fall below the ground-based results since the former can better isolate the target sources from other nearby sources (see Fig. 2 of Figer et al. 1999c).

2.6. Detailed comparison of SWS and CVF spectra

A comparison of the CVF and the SWS spectra is presented in Fig. 6. The SWS spectra were transformed to surface brightness using the measured aperture sizes, which are 1.12× and 1.29×, and 1.06× larger than the nominal apertures for Bands 1, 2, and 3, respectively (Salama, private communication). These factors, derived from beam profiles, are 0th order approximations of a parameter that is a function of wavelength. The change of correction factor introduces a ∼10% jump at the Band 1/Band 2 interface (4 μm), where the nominal aperture remains unchanged. The CAM spectra were extracted using a synthetic rectangular apertures approximating the *measured* apertures of SWS, and centered as shown in Fig. 1.

Over the 4–12 μm range, SWS Band 2, the agreement between the SWS and the CVF spectra is excellent for Q3, which is fairly isolated. The SWS spectrum of Q2 falls short of the CVF result; this difference is due to the fact that Q2 is near the edge of the SWS beam, where the responsivity is much lower than in the beam centre.

For Band 3, the SWS shows an increase in surface brightness for both spectra. No such increase is expected for Q3 on the basis of the CVF spectra, while a minor one is expected for Q2. The difference is likely to come from the detailed shape of the SWS beam profile, which is not accounted for in this simulation.

In Band 1 the CVF spectra show a rapid decrease with wavelength, which is unexpected and contrary to the SWS behaviour. We note that this region corresponds the the beginning of the CVF spectrum, where detector transient effects are most serious (no transient correction was applied to the SW data since the behaviour of these detectors was not sufficiently well characterised), and to the edge of the SW-CVF, where the determination of the response function is most uncertain. We consider this portion of the CVF spectra unreliable.

We conclude that, with the exception of the first part of the CVF spectrum, the agreement between the two datasets is excellent, and this suggests that the overall uncertainties could be less that ∼10% over most of the spectral range.

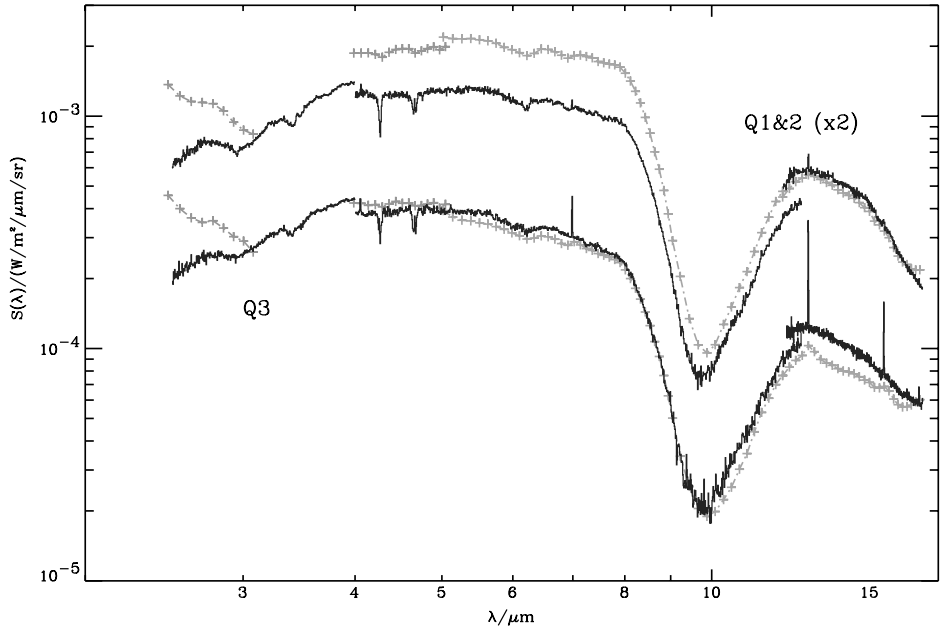

Fig. 6. Comparison of SWS spectra (black histogram) with spectra extracted from CVF images (grey crosses; different shades of grey indicate different CVF sections)

3. Results

3.1. Emission lines

One of the objectives of the SWS spectra of the cocoon stars was to search for emission lines that could clarify the nature of these stars. A careful search of the spectra has revealed only ionized hydrogen and forbidden lines attributable to the Pistol H II region. These are stronger in the spectrum of Q3, which is closer to the H II region so that more line (and continuum) emission is included in the SWS aperture. In contrast, only the strongest lines are detected in the Q2 spectrum, and these are detected mostly at the longest wavelengths, where the SWS aperture is largest. Furthermore, these lines are not detected in the CVF and Palomar spectra, albeit at lower resolution, confirming that they are not intrinsic to the cocoon stars. In contrast, these lines are clearly detected in the CVF and Palomar spectra of the Pistol H II region. Beyond 28 μm the spectra (not shown) were obtained with even larger apertures, and the contamination by the Pistol Nebula, both in terms of forbidden line emission and of thermal emission from the warm dust (Moneti et al. 2000), begins to dominate over the cocoon stars. Thus, no emission line attributable to the cocoon stars themselves was detected.

3.2. Dust and gas features

The spectra contain many dust absorption bands; these have been the subject of a number of recent studies (Schutte et al. 1998; Gerakines et al. 1999; Chiar et al. 2000), while Moneti & Cernicharo (2000) have studied the gaseous components (all these results come from the same SWS spectra used here). These results show that the lines of sight toward Q2 and Q3 contain (i) cold molecular cloud material, traced by absorption by cold ($\simeq$10 K) CO and H_2O gas and by various ice species (H_2O, CO_2, CO, and CH_4), and more tenuous ISM material, traced by aliphatic and aromatic hydrocarbon features. Special attention has been paid to the narrow absorption feature at 6.2 μm, attributed to the C–C stretch in aromatic hydrocarbons. Schutte et al. (1998) suggested that it could be the UIR feature seen in absorption, and justify the lack of absorption at 3.28 and 11.3 μm on excitation and temperature grounds, while they find that the observed spectrum is consistent with the presence of some absorption at 7.7 μm. The best detection of this absorption feature is toward WR118, a DWCL star whose absorption spectrum is believed to due to diffuse ISM material only, and marginal detections are reported towards three other DWCL stars (Schutte et al. 1998). Chiar et al. (2000), noting the 6.2 μm absorption in the cocoon stars, which might also be DWCL stars, suggested that this absorption feature could be associated with the environment of the DWCL stars rather than to the diffuse ISM. However, Chiar et al. (2000) also note that WC stars are not likely to be significant contributors to the carrier(s) of the C–H stretch (3.28 μm band), so that if the 3.28 and 6.2 μm bands (and the other UIR bands) are indeed connected, it is unlikely that they arise primarily in the surroundings of late-type WC stars.

In contrast to the cocoon stars, the CVF data clearly show the UIR bands in emission in the spectrum of the background, as shown in Fig. 7. The intensity of this emission is only $\sim$2 and 3% of the continuum of Q2 and Q3, respectively, which is weak compared to the measured absorption. The background emission also shows the forbidden lines of [Ar II] and [Ne II], and an important level of

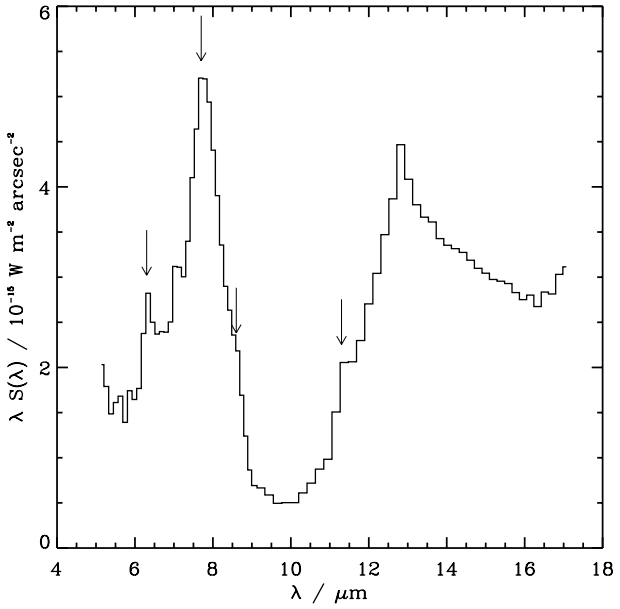

Fig. 7. The UIR features as seen in the spectrum of the background, in this case a 5×5 pixel region in the north-east corner of the array. The UIR features at 6.2, 7.7, 8.6, and 11.3 μm are identified by the arrows

continuum. A part of this emission could be due to light scattered within the instrument.

We have attempted to locate the source of the 6.2 μm emission from the CVF data by computing the difference of the line planes of the datacube minus the adjacent continuum planes. The result was flat, indicating that the emission is uniform over the whole region (unlike the [Ar II] and [Ne II] emission, which occur in the Pistol H II region). We deduce that the UIR emission is a characteristic of the line of sight rather than of the cocoon sources. We cannot determine where along the line of sight the UIR emission originate on the basis of our data.

3.2.1. The silicate features

The silicate absorption bands at 9.7 and 18 μm are the strongest features in the cocoon star spectra. We have used several published emissivity profiles to model the observed absorption. Most published profiles concern the 9.7 μm feature which is observable from the ground: Roche & Aitken (1984, RA84), Hanner et al. (1995, HBT95), Bowey et al. (1998, BAW98), while two determinations include both features: Pégourié & Papoular (1995) and Simpson (1991). The studies of RA84 and BAW98 are based on absorption of ISM dust, HBT95 study the absorption by molecular cloud dust, and the remainder are based on the dust emission around late type supergiant stars, which are generally believed to reproduce the ISM profile. These profiles, normalized to unity at their peak value, are shown in Fig. 8. A detailed comparison of these emissivities is beyond the scope of this work, but it is worth noting that there are important differences, even among those that should be very similar (e.g. the RA84 μ Cep profile and the Simpson 1991 group 1 profile, which is based on several stars with narrow 9.7 μm features, including μ Cep itself). Some of the differences should probably be ascribed to the different methods of determining and modeling the continuum, which will produce important differences in the wings of the profiles.

We removed the silicate features from the spectra by using the above emissivity profiles, $\epsilon(\lambda)$, as follows:

$$F(\lambda) = f(\lambda) \mathrm{e}^{\tau_{\mathrm{sil}} \epsilon(\lambda)}$$

where $F(\lambda)$ is the corrected spectrum, $f(\lambda)$ is the observed spectrum, and τ_{sil} is the peak optical depth of the feature. The best fitting profile and the peak optical depth were determined subjectively by requiring that the cleaned spectrum be continuous and free of residual features. The alternative of using χ^2 methods was considered, but the errors at the beginning and the end of the profiles produce large deviations in the corrected spectra, which hide the deviations caused by more important errors in the profile where the emissivity is large. This is particularly evident over the 9.7 μm feature, which is strong and narrow.

The best emissivity profile for the 9.7 μm feature is the μ Cep profile from RA84, and proper correction for all the sources is achieved with $\tau_{\mathrm{sil}} = 2.9 \pm 0.1$. The weak and sharp feature remaining at 9.4 μm is not real, but it is due to a slight error in the determination of the emissivity profile in a region of rapid variation and where the atmospheric absorption is greatest. A change of 0.1 in τ_{sil} produces a clearly noticeable effect in the corrected spectra.

The two 18 μm emissivity profiles are similar in shape but differ in strength relative to the 9.7 μm feature: Pégourié & Papoular (1985) determine $\tau(18)/\tau(9.7) = 0.35$, while Simpson (1991) constrained her continuum model to produce $\tau(18)/\tau(9.7) = 0.40$. We have used the Pégourié & Papoular (1985) profile multiplied by 1.15 to produce $\tau(18)/\tau(9.7) = 0.40$, and joined it to the RA84 μ Cep profile at 13 μm. We note that the Pégourié & Papoular (1985) profile of the 9.7 μm feature is much narrower than the cocoon star feature. This combined profile gives a deeper minimum at 12 μm than if we had used the Simpson (1991) profile alone. The corrected (and dereddened, see below) spectra, are shown in Fig. 8.

Our value of τ_{sil} is significantly higher than the value deduced by Schutte et al. (1998), who measured the depth of the feature relative to the level of the spectrum adjacent to the feature. While their method is fine for their purpose, which is to intercompare the variation of this and other features in several sources, their result does not account for the absorption at 12–14 μm, as seen in Fig. 8.

We are confident that our method is reliable for the 9.7 μm feature, but attempts to use to SWS spectra to place independent constraints on the strength and shape of the 18 μm feature using the same criteria adopted for the 9.7 μm feature proved unsuccessful. The reason is probably that beyond 18–20 μm these spectra are a blend of various cocoon stars and of the Pistol H II region, and are thus intrinsically too complicated for a subjective determination of a "smooth" spectrum. Furthermore, the

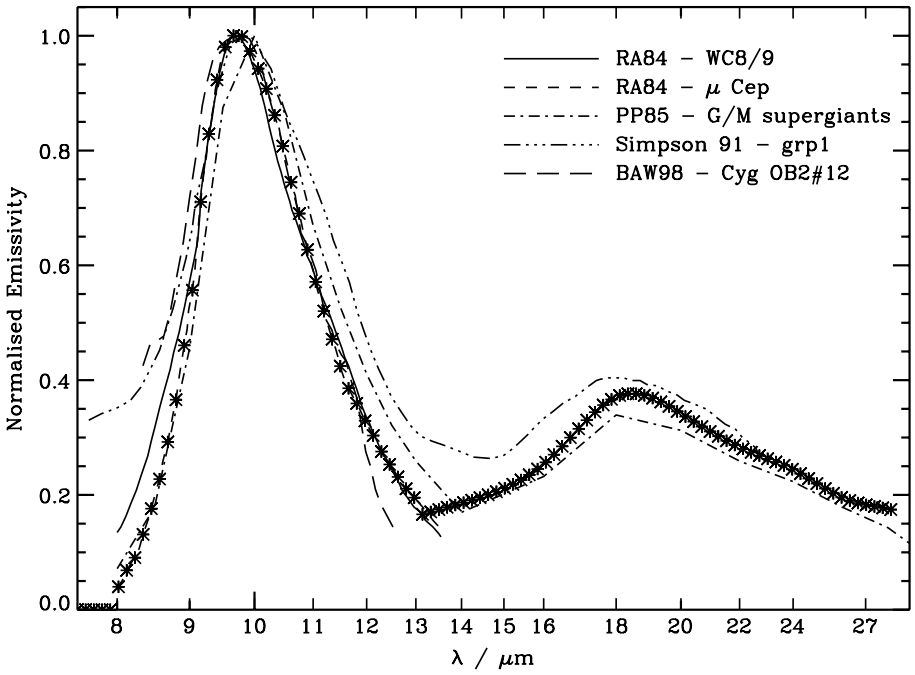

Fig. 8. Comparison of different published silicate emissivities. The adopted emissivity is traced by the black diamonds

task was intrinsically more difficult due to the weaker and broader nature of the 18 μm feature.

3.3. The extinction law

The extinction law, A_λ/A_V, toward the GC is known to give rise to more extinction than the standard law both in the silicate bands and in the 5–8 μm spectral range: Roche & Aitken (1985, RA85) have shown that $A_V/\tau_{\rm sil} \simeq 8.5$, or $A_K/\tau_{\rm sil} \simeq 0.70$ with their extinction law (van de Hulst No. 15), toward the GC, which is about half the value in the solar neighborhood; and Rieke et al. (1989) have shown on the basis of the Br-γ to Br-α ratios, that the extinction at 4 μm towards the GC is higher than expected with standard laws. These results were confirmed and extended by Lutz (1999) using hydrogen emission lines throughout the 2.5 to 12 μm range.

We have combined the above results to construct a reddening law appropriate for the GC as follows:

1. shortward of the 2.5 μm we follow the Rieke & Lebofsky (1985) law which was determined for GC sources. At $0.9\,\mu{\rm m} < \lambda < 2.5\,\mu{\rm m}$ this law can be approximated by a power law $A_\lambda \sim \lambda^{-\alpha}$, with $\alpha = 1.63$;
2. between 2.5 and 3.8 μm some structure is seen in the Lutz (1999) results which is due to the ice feature at 2.9 μm and to the amorphous carbon feature at 3.4 μm. We modeled these features as Gaussian;
3. at $\lambda \simeq 3.8$–8 μm, a power law with $\alpha = 0.35$, was used to approximate the results of Lutz (1999). Note that the point at 6 μm, where the deviation from the power law is largest, suffers extra extinction due to the water-ice feature. At the position of Br-α this law gives the same results as the Rieke et al. (1989);
4. between 8 and 24 μm, the silicate absorption features are modeled using the emissivity adopted in the previous section, with $\tau_{\rm sil} = 2.9$; and
5. beyond 24 μm a power law with $\alpha = 2$ is adopted (e.g. Draine & Lee 1984). In practice this last portion of the reddening law does not affect our results.

The adopted extinction law is shown in Fig. 9, where other commonly used reddening laws are shown for comparison, and it is tabulated in Table 3. With this law, $A_V/A_K = 8.9$, $A_V/\tau_{\rm sil} = 10$, and $A_K/\tau_{\rm sil} = 1.14$.

3.4. Extension of the cocoon stars

Inspection of the Palomar images (Fig. 4) shows significant extended emission around some of the cocoon stars. Figure 10 shows the radial profiles which were measured on a special mosaic composed from selected exposures of superior seeing obtained during a single night at each wavelength. The radial profile of the isolated, but rather faint star, X Sgr, that was observed at nearly the same airmass, is also shown for comparison (the profile of α Her observed at unit airmass, not shown, is even narrower, with a $FWHM = 0.69''$ vs. $0.59''$ for the diffraction size of $1.22\lambda/D$).

The profiles of Q3 and of Q4 (out to 1.5″, beyond which Q4 is likely to be contaminated by the bright sources nearby) are similar to that of reference star. Q1 and Q9 show wings that are almost 10× higher, while Q2 shows a weaker, but clear excess. The profiles shown are azimuthal averages, but the extensions are clearly asymmetric and do not show a common preferred direction, as seen in Fig. 4.

Could the observed profile wings be due to other nearby red stars? The high spatial resolution 2.05 μm

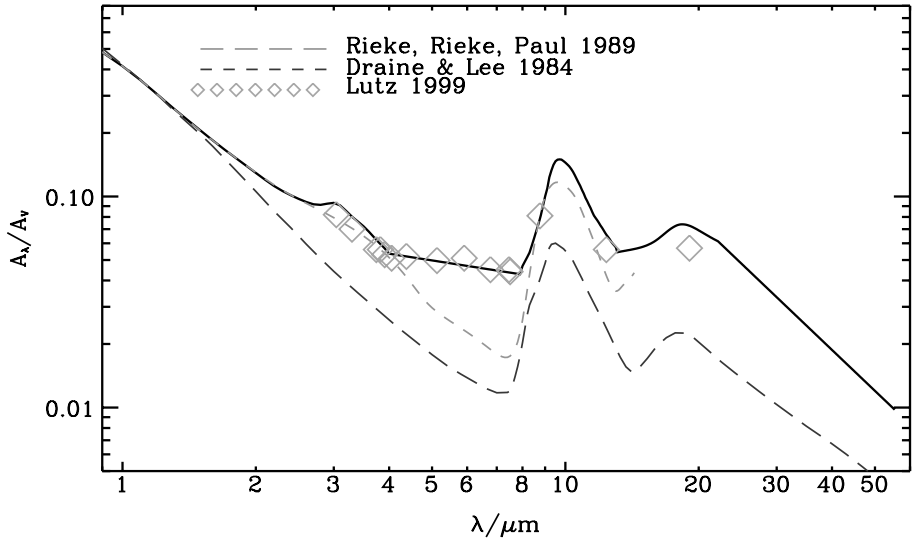

Fig. 9. Adopted extinction law compared to Draine & Lee (1984), Rieke et al. (1989), and Lutz (1999)

Table 3. The extinction law

$\lambda/\,\mu$m	A_λ/A_V	$\lambda/\,\mu$m	A_λ/A_V
0.55	1.0000	12.00	0.0721
0.65	0.7689	12.50	0.0634
0.80	0.5584	13.00	0.0569
1.00	0.4097	13.50	0.0545
1.25	0.2804	14.00	0.0553
1.65	0.1736	14.50	0.0561
2.20	0.1108	15.00	0.0573
2.50	0.0964	15.50	0.0589
3.00	0.0923	16.00	0.0612
3.50	0.0715	16.50	0.0643
4.00	0.0530	17.00	0.0677
4.50	0.0510	17.50	0.0707
5.00	0.0492	18.00	0.0726
5.50	0.0477	18.50	0.0730
6.00	0.0464	19.00	0.0721
6.50	0.0452	19.50	0.0704
7.00	0.0441	20.00	0.0683
7.50	0.0431	20.50	0.0663
8.00	0.0463	21.00	0.0644
8.50	0.0628	21.50	0.0626
9.00	0.0989	22.00	0.0610
9.50	0.1454	22.50	0.0586
10.00	0.1431	23.00	0.0561
10.50	0.1250	23.50	0.0537
11.00	0.1023	24.00	0.0515
11.50	0.0835	> 24.0	$\propto \lambda^{-2}$

(F205W) HST/NICMOS images of Figer et al. (1999) show three reddish stars close to Q1, a large blob of diffuse emission NW of Q2, weak but not red stars near Q3 and Q4, and a fairly isolated Q9. The blob near Q2, the brightest of the group, is likely to be an artifact. We have performed photometry of all the "companions", and find that the red ones are far less red than the cocoon stars, and simple extrapolations of their energy distributions to 8 and 12 μm would produce negligible flux at those wavelengths. Also, we note that Q9, which is the most extended cocoon star, is also the most isolated in the near IR. We therefore conclude that Q1, Q9, and to a lesser extend Q2 are intrinsically extended. At the distance of the Galactic Centre (8 kpc), an angular radius of $2''$ corresponds to a physical radius of 0.08 pc or 16 000 AUs (radius to zero power). The true radius should be somewhat smaller, given the seeing of $\simeq 1''$ for the observations, but will remain nevertheless very important.

3.5. Energy distributions and luminosities

Using the reddening law constructed above we dereddened our spectra assuming $A_K = 3.3$ mag ($A_V = 29$ mag), as determined by Figer et al. (1998) from the average color excesses of the early-type stars in the cluster. The uncertainty in A_V is 5 mag. The results are shown in Fig. 11 together with the dereddened ground-based data of FMM99 and of Okuda et al. (1990)

The resulting SEDs were modeled in three ways (see also Fig. 11):

1. a constant temperature, optically thick shell, modeled by a Planck function (dot-dash lines in Fig. 11);
2. a constant temperature, optically thin shell, modeled by a Planck function multiplied by a λ^{-1} emissivity law: this produces an energy distribution narrower than the optically thick models (not shown);
3. an optically thin but geometrically thick dust shell with r^{-2} density law (constant velocity wind) as used by WHT to model known DWCL stars. The shape of the model SED is determined by the dust temperature, T_0, at the inner radius of the shell, R_0, and the shell thickness, H, which is measured in units of R_0. A dust emissivity proportional to λ^{-1} was used. This model produces an SED that is wider than a Planck function modified with the same emissivity law, and

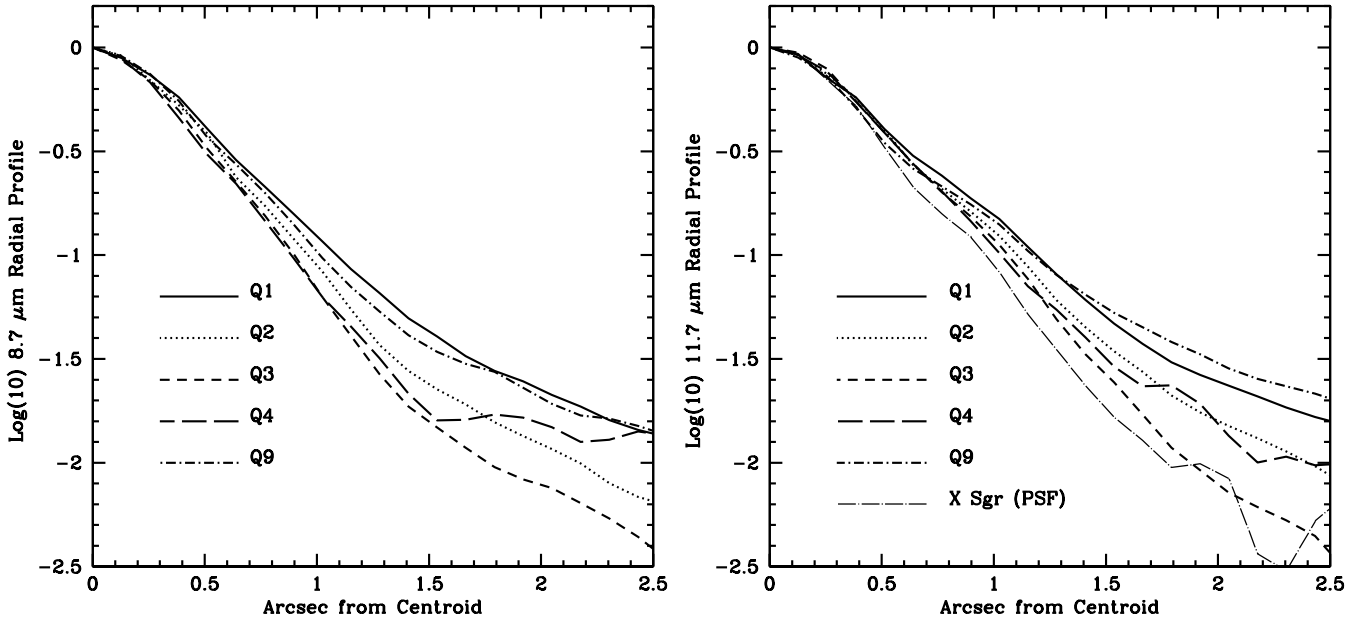

Fig. 10. Radial profiles of the cocoon stars at 8.7 and 11.7 μm. The profile of the reference star X Sgr at 12 μm is also shown for comparison. All observations were obtained at airmass $\simeq 2.2$

Table 4. Model parameters and results

Source	$T_{\rm BB}$	T_0/K	H	$\log(L/L_\odot)$
Q1	500	550	100	4.5
Q2	625	675	50	4.9
Q3	650	700	50	4.6
Q4	725	775	50	4.1
Q9	400	425	100	4.7

whose width increases as the physical thickness increases (solid line in Fig. 11).

More detailed models of the DWCL dust shells have been computed by Zubko et al. (1998). While those models provide useful new results on the properties of the dust, the SEDs they produce are not significantly different from those of WHT, so we will stay with the WHT models for the remainder of this work.

The models described above were normalized to the data at λ between 6.5 and 7 μm, where the spectrum is reasonably free of dust or ice absorption features. The model parameters are listed in Table 4. In all cases the shell thickness is very large, and increasing H further does not have a significant effect on the SED, thus these models only place a lower limit to the shell thickness. A change of 20 K in T_0 produces a significant change in the SED, and the value of 20 K can be taken as the uncertainty in T_0.

As can be seen in the Fig. 11, the DWCL-like models can reproduce quite well the SEDs over the 4–17 μm range. The models reproduce best the SEDs for Q2, which is the brightest in the mid-IR, and Q3, which is the most isolated source. Q1 is not very bright at long λ, and its spectrophotometry is likely to suffer some contamination from the nearby Q2, especially from the first Airy ring of the PSF of the latter. Q4 also suffers heavy contamination by the nearby sources, as described in Sect. 2.5. Q9 is the the reddest source, its SED is somewhat peculiar, possibly due to some contamination at short λ; for this source the model is mediocre at best.

Below $\simeq 4$ μm the model SEDs fall far below the observations, suggesting that the actual hot dust contribution is larger than in the model. Luminosities were computed integrating underneath the model SEDs; they are $10^{4.1}$ to $10^{4.9} L_\odot$ for the DWCL-like models, while the blackbody models give luminosities about 0.1 dex lower (see Table 4). These values do not differ significantly from previous determinations.

4. Discussion

4.1. The origin of the absorption features

Combining the adopted value of A_V with the value of $\tau_{\rm sil} = 2.9 \pm 0.1$ determined in Sect 3.2, gives $A_V/\tau_{\rm sil} \simeq 10 \pm 2$. This, within the uncertainties, is equal to the nominal value of 8.5 determined by RA85 for the sources near Sgr A*. This implies that all the silicate absorption, and by extension all the extinction, takes place along the line of sight. This is not surprising: the infrared polarisation toward the cocoon stars and toward Sgr A* is about the same both in amount and in position angle (Kobayashi et al. 1983), and the depths of the other ice and gas features are all similar to, though usually slightly lower than, their corresponding values toward Sgr A* (Gerakines et al. 1999; Chiar et al. 2000; Moneti & Cernicharo 2000). The general conclusion is that there is slightly less absorbing material toward the Quintuplet Cluster than toward Sgr A*, and also that the fraction of cold molecular cloud

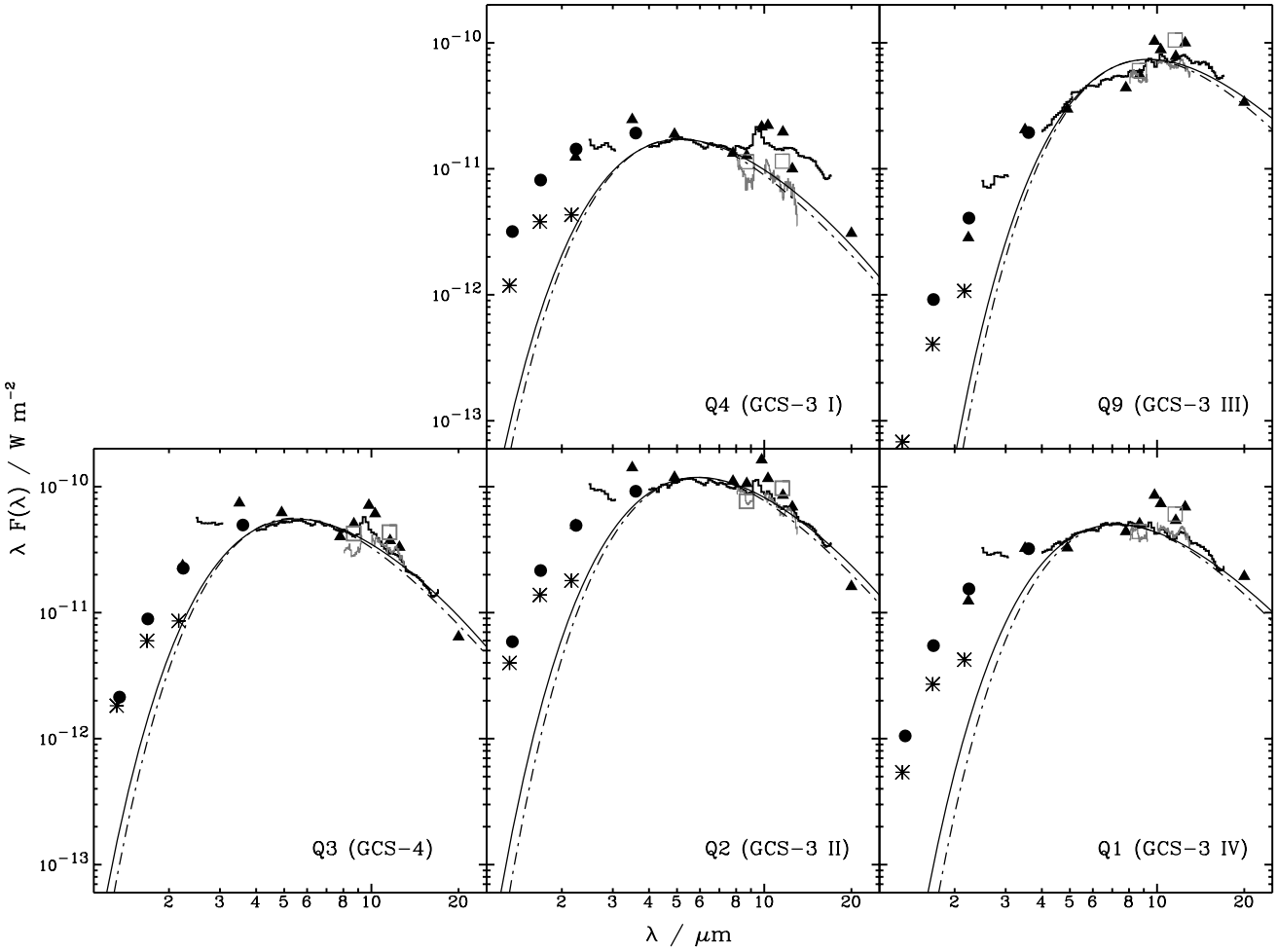

Fig. 11. Dereddened spectral energy distributions of cocoon stars; symbols are as in Fig. 5. The models shown are simple blackbodies (dot-dash lines) and DWCL-like shells (solid lines)

material is lower toward the cluster. All this speaks against any absorption being produced by the cocoon stars themselves, and supports the conclusion that all the absorption features observed are of interstellar origin.

The lack of intrinsic absorption speaks against the interpretation of the cocoon stars as deeply embedded YSOs, where the deep silicate absorption is ascribed to the molecular cloud in which the YSO is deeply embedded. Furthermore, the 9.7 μm feature toward deeply embedded YSOs is usually broader than that of the ISM, and is better reproduced by the Trapezium profile than by the μ Cep profile. Also, the spectra of embedded YSOs usually show warm CO and H_2O gas in absorption (see, e.g. van Dishoeck & Helmich 1996), presumably arising in a region where this gas is warmed either by the young stars itself or by shocks produced when the wind and/or the outflow from a young stars strikes the surrounding molecular material. No such warm gas is found toward the cocoon stars. Indeed, molecular line studies have shown the Quintuplet Cluster is located in a region free of molecular gas (Serabyn & Güsten 1991).

4.2. On the DWCL hypothesis

The luminosities derived in Sect. 3.5 are those of the shells. The total stellar luminosity, assuming that the shell absorbs and emits isotropically, will be the sum of the observed (and dereddened) shell luminosity and the observed (and dereddened) stellar luminosity, the latter being that fraction of the stellar luminosity not absorbed by the shell, and transmitted toward the observer. In the following we will always refer to these observational quantities.

For most of the DWCL stars studied by WHT, the ratio of shell to stellar luminosity is $\lesssim 0.1$, while only for the most extreme 20% it is between 0.5 and 0.7. Assuming the lower value, i.e. $L_{\rm shell}/L_{\rm star} = 0.1$, the total luminosities of the cocoon stars would be comparable to those of typical Galactic and Magellanic Clouds WCL stars, $\sim 10^{5.5} L_{\odot}$. But the lack of near IR spectral lines (especially in the J-band, see FMM99) suggests that $L_{\rm shell}/L_{\rm star}$ must be large. If half the total stellar luminosity were re-emitted by the shell, and, for the sake of argument, if they were both Planckian with effective temperatures of 25 000 and 800 K respectively, then the two energy distributions would intersect at $\simeq$1.37 μm, and the 1.25 μm continuum of the star would be $\sim$ 3$\times$ that of the shell. In this

situation, the ratio $L_{\rm shell}/L_{\rm star} = 1.0$, already larger than for the most extreme DWCL stars in WHT. Increasing the stellar temperature to 35 000 K will move the intersection point to 1.27 μm, and the stellar continuum will be only 20% higher than the shell continuum. Under such circumstances the stellar emission line spectrum should still be easily visible in the J-band, unlike the results of FMM99. Increasing the shell luminosity to 10× the (transmitted) stellar luminosity would be necessary for the shell continuum to dominate the stellar continuum at 1.25 μm. Thus, for the J-band spectrum to be dominated by the shell, the shell luminosity would have to be $\gtrsim 90\%$ of the total (shell + star), and the star has to be very hot. In this case, the UV optical thickness of the shells would have to be much greater than unity, which would probably be inconsistent with the optically thin shell in the near and mid IR, but it would bring the total luminosities roughly equal to the observed luminosities, and these values are rather low for typical DWCL stars.

In summary, if the shells reprocess only a small part of the true stellar luminosity, then the true stellar luminosity is comparable to that of known DWCL stars, but the stellar spectrum should be observable in the J-band. If, on the other hand, the shells reprocess most of the luminosity of the central star, in which case our models are likely to fail on optical thickness grounds, our models predict a total luminosity much lower than known DWCL stars.

The physical size of the shells can be estimated from their luminosity and $T_{\rm BB}$. Taking typical values of $L = 50\,000\,L_\odot$ and $T_{\rm BB} = 500$ K, we derive a physical diameter of 250 AU, which corresponds to and angular diameter of 35 milliarcsec. This value should correspond roughly to the inner diameter of the shell. The outer diameter will be 50–100× larger, or $\simeq 2$–$3''$. These values are very rough, but they are overall consistent with the observed extensions observed in the Palomar images, though the coincidence could be fortuitous.

4.3. Other interpretations

Glass et al. (1999) suggested that the cocoon stars could be self-enshrouded massive stars of the type suggested by Bernasconi & Maeder (1996). Without discussing those models, we note that the measured shell luminosities in Table 4, if they represent the total stellar luminosity, correspond to stars of initial mass between 15 and 25 $M_\odot$ in the theoretical HR diagrams of Bernasconi & Maeder (1996). This would place them below the $\simeq$40 $M_\odot$ limit of the stars that would remain obscured on the Main Sequence if those models were applicable. Secondly, if the cocoon stars are coeval with the rest of the cluster, their age of $\simeq$4 Myrs would make them too old for this proposed evolutionary stage.

Okuda et al. (1990) already discussed why other evolved stars are unlikely explanations of the nature of the cocoon stars. We add here that the luminosities we derived are somewhat too high for AGB stars, and also that the cluster is too young for AGB stars to have formed: stars much more massive than $\sim$8 $M_\odot$ are still on the main sequence (FMM99).

5. Conclusions

New mid-infrared spectroscopic observations of the enigmatic cocoon stars in the Quintuplet Cluster were obtained in order to put further constraints on their nature. The high spectral/low spatial resolution spectroscopy did not reveal any feature that could be assigned to the cocoon stars themselves. The low spectral/high spatial resolution spectrophotometry was used to study the form of the silicate absorption in these stars, and we conclude that (i) the depth of the absorption is the same for all the stars, and (ii) there is no evidence for any silicate emission or absorption intrinsic to the cocoon stars. In fact, all of the absorption features are consistent with an origin in the molecular clouds and in the more tenuous ISM along the line of sight.

We have examined carefully the hypothesis that the cocoon stars are extreme DWCL stars. The SEDs of the cocoon stars can be reproduced by the models of DWCL shells presented by WHT, but the high UV optical thickness needed to reprocess most of the luminosity of the central star suggests that these models might not be applicable to such extreme stars. Furthermore, the luminosities derived are significantly lower than those of known DWCL stars, and also these stars are extremely rare in the Galaxy, though they are concentrated in the GC. Yet, stars of the carbon sequence are necessary to produce featureless spectra.

The new observations do not provide any new constraints in favour of any of the proposed identifications of the cocoon stars but they do provide new arguments against all three of the main hypotheses that have generally been considered, namely dust-enshrouded youg stars, late-type (OH/IR or AGB) stars, or late-type WC stars. The nature of these stars remains an enigma.

Acknowledgements. We would like to thank T. Hayward and T. Herter for assistance in obtaining and reducing the SpectroCam-10 data and Cornell University for providing access to the Hale telescope. S.R.S. acknowledges support by NASA grant NAG2-207 and NSF grant AST-9218038. NASA grants NAGW-2551 and NAGW-2870 supported the development of SpectroCam-10 and the detector.

References

Bernasconi, P. A., & Maeder, A. 1996, A&A, 307, 829
Biviano., A., Altieri, B., Blommaert, J. A. D. L., et al. 1997, in First ISO Workshop on Analytical Spectroscopy, ed. A. M. Heras, K. Leech, N. R. Trams, & M. Perry, ESA-SP419, 61
Cesarsky, C. J., Abergel, A., Agnèse, P., et al. 1996, A&A, 315, L32
Chiar, J. E., Tielens, A. G. G. M., Whittet, D. C. B., et al. 2000, ApJ, 537, 749

Cohen, M., Walker, R. G., Barlow, M. J., & Deacon, J. R. 1992, AJ, 104, 1650, 1992
Draine, B. T., & Lee, H. M. 1984, ApJ, 285, 89
de Graauw, T., Hase, L. N., Beintema, D. A., et al. 1996, A&A, 315, L49
de Graauw, T. 1999, in The Universe as seen by ISO, ed. P. Cox, & M. Kessler, ESA-SP427, 31
Figer, D. F., Najarro, F., Morris, M., et al. 1998, ApJ, 506, 384
Figer, D. F., McLean, I. S., & Morris, M. 1999a, ApJ, 514, 202 [FMM99]
Figer, D. F., Morris, Geballe, T. R., et al. 1999b, ApJ, 525, 759
Figer, D. F., Kim, S. S., Morris, M., Serabyn, E., Rich, R. M., & McLean, I. S. 1999c, ApJ, 525, 750
Gerakines, P. A., Whittet, D. C. B., Ehrenfreund, P., et al. 1999, ApJ, 522, 357
Glass, I. S., Catchpole, R. M., & Whitelock, P. A. 1987, MNRAS, 227, 373
Glass, I. S., Moneti, A., & Moorwood, A. F. M. 1990, MNRAS, 242, 55p [GMM90]
Glass, I. S., Matsumoto, S., Carter, B. S., & Sekiguchi, K. 1999, MNRAS, 304, L10
Hanner, M. S., Tokunaga, A. T., Veeder, G. J., & A'Hearn, M. F. 1984, AJ, 89, 162
Hanner, M. S., Brooke, T. Y., & Tokunaga, A. T. 1995, ApJ, 438, 250
Hayward, T. L., Miles, J. W., Houck, J. R., Gull, G. E., & Schoenwald, J. 1993, Proc. SPIE, 1946, 334
Kessler, M. F., Steinz, J. A., Anderegg, M. E., et al. 1996, A&A, 315, L27
Kobayashi, Y., Okuda, H., Sato, S., Jugaku, J., & Dyck, H. M. 1983, PASJ, 35, 101
Moneti, A., Glass, I. S., & Moorwood, A. F. M. 1992, MNRAS, 258, 714 [MGM92]
Moneti, A., Glass, I. S., & Moorwood, A. F. M. 1994, MNRAS, 268, 194 [MGM94]
Moneti, A., Blommaert, J. A. D. L., Najarro, F., Figer, D., & Stolovy, S. 1999, in The Universe as Seen by ISO, ed. P. Cox, & M. Kessler, ESA SP-427, 723
Moneti, A., Blommaert, J. A. D. L., Crowther, P., et al. 2000, in preparation
Moneti, A., & Cernicharo, J. 2000, in ISO beyond the peaks, ed. A. Salama, M. F. Kessler, K. Leech, & B. Schulz, ESA SP-456, in press
Nagata., T., Woodward, C. E., Shure, M., Pipher, J. L., & Okuda, H. 1990, ApJ, 351, 83
Nagata, T., Kawara, K., Onaka, T., Kitamura, Y., & Okuda, H. 1996, A&A, 315, L205
Lutz, D. 1999, The Universe as Seen by ISO, ed. P. Cox, & M. F. Kessler, ESA-SP 427, 623
Okuda, H., Shibai, H., Nakagawa, T., et al. 1990, ApJ, 351, 89
Pégourié, B., & Papoular, G. 1985, A&A, 142, 451
Rieke, G. H., & Lebofsky, M. J. 1985, ApJ, 288, 618
Rieke, G. H., Rieke, M. J., & Paul, A. E. 1989, ApJ, 336, 752
Roche, P. F., & Aitken, D. K. 1984, MNRAS, 208, 481 [RA84]
Roche, P. F., & Aitken, D. K. 1985, MNRAS, 215, 425
Schutte, W. A., van der Hucht, K. A., Whittet, D. C. B., et al. 1998, A&A, 337, 261
Serabyn, E., & Güsten, R. 1991, A&A, 242, 376
Simpson, J. P. 1991, ApJ, 368, 570
van Dishoeck, E. F., & Helmich, F. P. 1996, A&A, 315, L177
Williams, P. M., van der Hucht, K. A., & Thé, P. S. 1987, A&A, 182, 91 [WHT]
Zubko, V. G. 1998, MNRAS, 295, 109